Biosensors and Bioelectronics 126 (2019) 381–388

Contents lists available at ScienceDirect

Biosensors and Bioelectronics

journal homepage: www.elsevier.com/locate/bios

Simple, low-cost, sensitive and label-free aptasensor for the detection of cardiac troponin I based on a gold nanoparticles modified titanium foil

Nasrin Siraj Lopa, Md. Mahbubur Rahman*, Faiz Ahmed, Taewook Ryu, Sabuj Chandra Sutradhar, Jin Lei, Jaewoong Kim, Dae Ho Kim, Yong Hoon Lee, Whangi Kim*

Department of Energy and Materials, Konkuk University, Chungju 27478, Republic of Korea

ARTICLE INFO

Keywords:
Gold nanoparticles
Ti foil
Cardiac troponin I
Aptamer
Label-free
Differential pulse voltammetry

ABSTRACT

This research demonstrated the electrochemical modification of low-cost titanium (Ti) metal substrate with gold nanoparticles (AuNPs) for the aptamer-based detection of cardiac troponin I (cTnI). AuNPs were deposited onto Ti sheets by the potential-step deposition method with high density and homogeneity as well as good crystallinity. It was then applied as a transducer to immobilize a thiol-functionalized DNA aptamer via the self-assembled monolayer mechanism for the specific binding of cTnI. This was verified through electrochemical and morphological analyses. The aptasensor could detect cTnI in a linear range of 1–1100 pM with a detection limit of ca. 0.18 pM. The aptasensor showed high sensitivity and specificity to cTnI over other interfering compounds with good recoveries in the diluted human serum samples.

1. Introduction

The world health organization (WHO) recently listed cardiovascular diseases (CVDs), including coronary artery diseases (CADs), hypertensive heart diseases, and heart failure, as the number one cause of death globally (Mendis et al., 2011). It has been estimated that about 17.7 million people died from CVDs in 2015, which accounts for about 31% of global deaths in that period (Ritchie and Roser, 2018). Among them, approximately 7.4 million people have died due to CADs, including angina, acute myocardial infarction (AMI), unstable angina pectoris, and heart failure (Ritchie and Roser, 2018). AMI in particular is the leading cause of death for CAD-affected people and a total of about 15.9 million cases of AMI occurred globally in 2015 (GBD 2015 Disease and Injury Incidence and Prevalence Collaborators, 2016). The age- and sex-adjusted incidence rate of AMI is 200 case/person-year (Jo et al., 2015). Thus, the development of a rapid, accurate, and low-cost diagnostic tool for AMI has attracted massive interest to the scientist and industrialist. Conferring the WHO guideline, AMI can be diagnosed by measuring variations in electrocardiography (ECG) signals, typical chest pain, and the concentrations of cardiac biomarkers in body fluids (Yang and Zhou, 2006; Tuteja et al., 2016). Among the various AMI diagnostic tools, ECG is the most popular. Nevertheless, a high percentage of AMI patients exhibit non-diagnostic ECG or ambiguous readings (Brady et al., 1999). Further, chest pain is not always an indication of AMI alone. Therefore, measuring the concentration of cardiac biomarkers in body fluids is an effective method for the diagnosis of AMI with high accuracy and precision. Several cardiac biomarkers such as cardiac troponin I (cTnI), myoglobin (Mb), C-reactive protein (C-RP), and creatine kinase-MB (CK-MB) have attracted interest as potential biomarkers for diagnosing AMI (Christenson and Christenson, 2013). cTnI is a potential biomarker due to its high specificity and sensitivity towards AMI compared to other biomarkers (Jo et al., 2015). Additionally, cTnI is released into the blood circulation immediately after AMI (Davies et al., 1991; Korff et al., 2006). Hence, the development of a rapid, accurate, low-cost, and sensitive method for the detection of cTnI in body fluids is potentially important.

Electrochemical methods are well suited for the rapid and sensitive detection of cTnI over conventional expensive, time-consuming, and low sensitive enzyme-linked immunosorbent assay (ELISA), electrochemiluminescence immunoassay (ECLIA), and piezoelectric immunoassay (Jo et al., 2015; Rezaee et al., 2017; Tang et al., 2018; Fonseca et al., 2011). Additionally, electrochemical methods have the advantages of short reading time, miniaturization ability, and requiring only a small amount of sample (Lopa et al., 2018a, 2018b). Numerous reports have been published on the electrochemical detection of cTnI based on the selective antibody-antigen interaction (Ko et al., 2007; Ahammad et al., 2011; Han et al., 2016). These antibody-based electrochemical systems have several limitations, which arise from the inherent properties of antibodies, including low-stability at high temperature, high-cost, short-shelf life, difficulty of modification, poor

* Corresponding authors.
E-mail addresses: mahbub1982@kku.ac.kr (Md. M. Rahman), wgkim@kku.ac.kr (W. Kim).

https://doi.org/10.1016/j.bios.2018.11.012
Received 24 August 2018; Received in revised form 26 October 2018; Accepted 10 November 2018
Available online 13 November 2018
0956-5663/

reusability, high immunogenicity, and low bioavailability (Tombelli et al., 2005). Recently, aptamers, which are peptide molecules or oligonucleic acids, have attracted massive interest for overcoming these limitations of antibodies. This is due to the superior characteristics of aptamers such as small size, high stability, low-immunogenicity, long-shelf-life, ease of synthesis, and low-cost (Tombelli et al., 2005). Aptamers are highly suitable for the development of electrochemical biosensors, owing to their ability to form unique three-dimensional (3D) structures to bind to the target specific biomolecules (Jo et al., 2015; Min et al., 2008; Maehashi et al., 2007). Additionally, the simple and easy chemical functionalization of aptamers enables their facile immobilization onto the electrode surfaces.

The modification of electrode surfaces with a high surface area and chemically stable nanomaterials is vital to maximizing the number of immobilized aptamers. This can enhance the sensitivity of the cTnI detection with a low limit of detection (LOD). A few reports are available for the aptamer-based electrochemical detection of cTnI based on a conventional Au electrode (AuE), Au nanodumbbells-modified AuE, and nitrogen-doped reduced graphene oxide modified glassy carbon electrode (GCE) (Jo et al., 2015; Negahdary et al., 2017; Chekin et al., 2018). Even though these reports attained good sensitivity and low LOD, they have the disadvantages of high cost, difficulty of miniaturization, and point-of-care testing (POCT). This is due to the utilization of precious and bulk AuE and GCE. Jo et al. (2017) further developed a hydrazine labeled aptasensor to detect cTnI based on the Au nanoparticle (AuNPs) and conducting poly (5,2′:5′2′-terthiophene-3′-carboxylic acid) modified screen-printed carbon electrode (SPCE). This portable and disposable SPCE-based aptasensor might offer the POCT of AMI with low-cost. However, controlling the homogeneity of the AuNPs surface with reliable reproducibility, complex fabrication steps, and the utilization of labeling are huge concerns for the future commercialization of this aptasensor. Hence, there is scope to investigate other conducting substrates with low-cost, high-stability, wide electrochemical potential window, and ease of modification with nanomaterials to detect cTnI without labeling.

In this research, we developed a AuNPs-modified titanium (Ti) metal foil (AuNPs/Ti) for the first time for the label-free detection of cTnI, as shown in Fig. 1. This label-free cTnI detection method is facile and simple, since it does not require any redox-active labeling, but instead measures the changes in the electronic or interfacial properties induced by the binding of cTnI with aptamers. AuNPs were deposited onto Ti by the potential step deposition method. The homogeneous distribution of the AuNPs onto the Ti electrode allows for the immobilization of a thiol-functionalized DNA aptamer for the target-specific binding of cTnI with high sensitivity and low LOD.

2. Experimental section

2.1. Chemicals

cTnI from a human heart, gold (III) chloride hydrate, human serum, bovine serum albumin (BSA), insulin (Ins.) from a porcine pancreas, cholesterol (Chol.), Mb, glucose oxidase (GO_x), immunoglobin G (IgG) from human serum, sodium dihydrogen phosphate (NaH_2PO_4), disodium hydrogen phosphate (Na_2HPO_4), potassium ferricyanide ($K_3[Fe(CN)_6]$), potassium ferrocyanide ($K_4[Fe(CN)_6]$), and titanium foil (99.7% purity) with the thickness of 0.25 mm were purchased from Sigma-Aldrich (St. Louis, Missouri, USA). A thiol functionalized DNA aptamer at the 5′ end with the sequence of 5′-CGTGCAGTACGCCAAC CTTTCTCATGCGCTGCCCCTCTTA-3′ for target-specific binding of cTnI (Jo et al., 2015) was purchased from Bio Basic (Ontario, Canada). A phosphate buffer solution (PB) of pH 7.0 was prepared according to our previously reported procedure (Lopa et al., 2018a, 2018b) and used throughout the experiment unless otherwise stated.

2.2. Instruments and measurements

All electrochemical measurements were carried out with a multichannel potentiostat (Ivium-n-Stat, Ivium Technologies, The Netherlands) using a conventional three-electrode system. Bare Ti foil and AuNPs/Ti were used as working electrodes. The reference and counter electrodes were Ag/AgCl (*aq.* saturated KCl) and platinum (Pt) wire, respectively. Differential pulse voltammograms (DPVs) were attained with the pulse width, pulse amplitude, and pulse period of 2 ms,

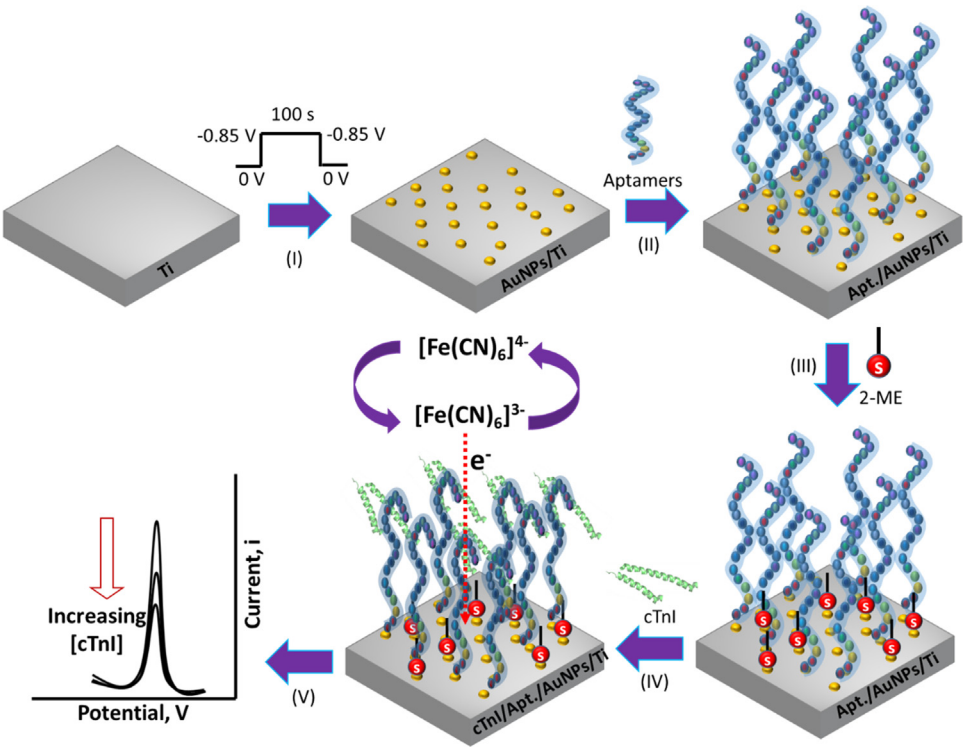

Fig. 1. Schematic illustration for the fabrication steps of the cTnI aptasensor: (I) electrodeposition of AuNPs onto Ti electrode by potential step method at − 0.85 V, (II) immobilization of aptamers, (III) blocking the sensor surface with 2-ME, (IV) binding of cTnI, and (V) detection of cTnI using $[Fe(CN)_6]^{3-/4-}$ redox couple solution in PB (pH 7.0) by DPV.

100 mV s^{-1}, and 100 ms, respectively. The electrochemical impedance spectra (EIS) were measured in the frequency range of (10^6–0.1) Hz with the ac amplitude of 5 mV (IM6ex, Zahner-Elektrik GmbH & Co. KG). Z-view software (version 3.1, Scribner Associates Inc., U.S.A.) was used to fit the EIS spectra. An X-ray diffractometer (D2 Phaser with Cu Kα radiation, Bruker), a field emission scanning electron microscope (FE-SEM, JEOL 7401F), and an energy dispersive X-ray spectroscopy (EDS, INCAx-sight 7421, Oxford Instruments) was used to characterize the crystallographic pattern, surface morphology, and elemental analysis, respectively. An atomic force microscope (Nanoscope, Bruker, Germany) in a non-contact mode was used to analyze the surface topography. A high-resolution transmission electron microscope (HR-TEM, Philips, CM 200) was used to investigate the morphology, selected area diffraction pattern (SAED), and the lattice fringes. The surface states were analyzed by X-ray photoelectron spectroscopy (XPS) (Thermo Scientific™ K_α, Thermo Fisher Scientific, UK) with a monochromatic Al K_α source. The optical absorption spectrum of AuNPs was obtained using a UV–Visible spectrophotometer (Perkin Elmer, Lambda 35, USA).

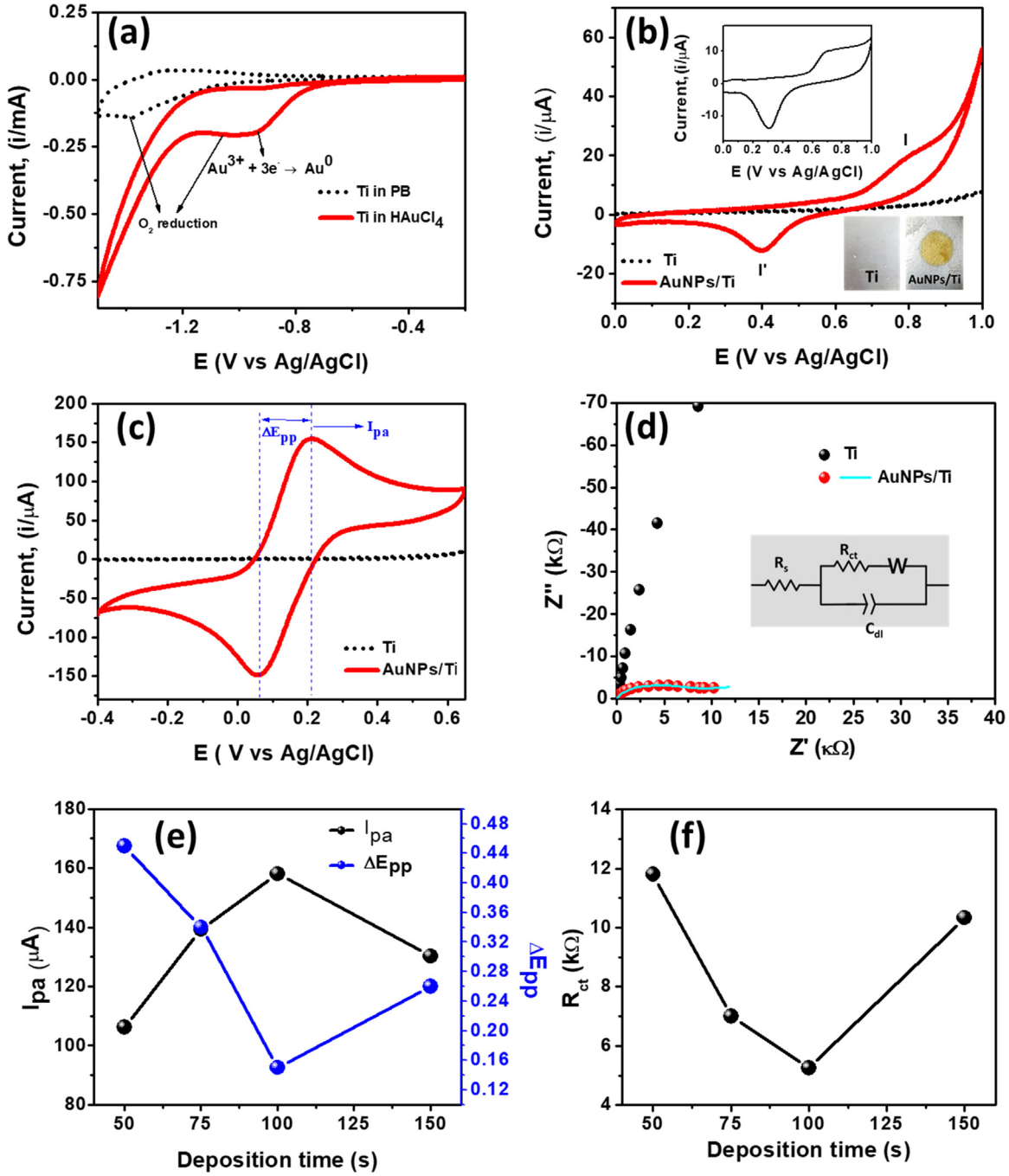

Fig. 2. (a) Cyclic voltammograms (CVs) of bare Ti in PB (pH 7.0) and $HAuCl_4$ (10 mM) solution in PB (pH 7.0). (b) CVs of bare Ti and AuNPs/Ti electrodes in PB (pH 7.0) with the AuNPs deposition time of 100 s (upper inset shows the CV of regular AuE and the lower inset shows the photographic images of Ti and AuNPs/Ti electrodes). (c) CVs and (d) EIS spectra (inset shows the Randles equivalent circuit model to fit the EIS spectra, which includes electrolyte resistance (R_s), R_{ct}, W, and double layer capacitance (C_{dl})) of Ti and AuNPs/Ti electrodes in $[Fe(CN)_6]^{3-/4-}$ in PB (pH 7.0). The symbols and solid lines in the EIS spectra designate the experimental and fitted data, respectively. Variations of the (e) I_{pa} and ΔE_{pp}, and (f) R_{ct} of $[Fe(CN)_6]^{3-/4-}$ redox couple at the AuNPs/Ti electrodes with varying deposition time. All of the CVs were measured at a scan rate of 100 mV/s.

2.3. Electrodeposition of AuNPs onto Ti foil

Prior to the deposition of AuNPs, Ti foil ($20 \times 25\,mm^2$) was sequentially cleaned by sonication with Alconox® detergent solution (Sigma), ethanol, and acetone, then dried by N_2 gas. Next, the sheet of Ti was installed into a Teflon cell with 10 mM $HAuCl_4$ solution in PB (pH 7.0). The exposed geometric area of the cell was ca. $0.32\,cm^2$. AuNPs were then deposited onto the Ti sheet by the potential step deposition method at − 0.85 V with the deposition time of 50, 75, 100, and 150 s.

2.4. Immobilization of aptamers and binding of cTnI

The AuNPs/Ti electrode was dipped into the SH-functionalized DNA aptamer solution (1 mL, 1 μM) in PB (pH 7.0) for 10 h at 4 °C. This allowed for the immobilization of aptamers onto the AuNPs surface via a self-assembled monolayer (SAM) mechanism. Then, the aptamers-modified AuNPs/Ti electrode (Apt./AuNPs/Ti) was washed with PB (pH 7.0) and dried. Subsequently, a blocking reagent of 2-mercaptoethanol (0.2 mM in ethanol) was added to the surface of Apt./AuNPs/Ti to minimize the nonspecific binding of cTnI. Varying concentrations of cTnI in PB (pH 7.0) were applied onto the Apt./AuNPs/Ti sensors at 37 °C for 50 min (Jo et al., 2017). Finally, the unbound cTnI was removed by washing with PB (pH 7.0), and the electrochemical measurements were carried out with a mixture solution of potassium ferro/ferri-cyanide ($K_4[Fe(CN)_6]/K_3[Fe(CN)_6]$) (5 mM each) redox couple in PB (pH 7.0).

3. Results and discussion

3.1. Electrochemical characterization of the AuNPs/Ti electrode

Fig. 2a shows the cyclic voltammograms (CVs) of Ti electrode in PB (pH 7.0) and 10 mM $HAuCl_4$ in PB (pH 7.0) in the potential scan range from − 0.2 to − 1.50 V at a scan rate of 100 mV/s. Ti electrode showed a cathodic wave at ca. − 1.37 V in the CV during a negative potential in PB (pH 7.0). This can be ascribed to the oxygen reduction reaction at Ti foil (Bakir et al., 2011). In contrast, the Ti electrode in $HAuCl_4$ solution exhibited a wide reduction wave, with cathodic peaks at ca. − 0.95 and − 1.05 V, as measured by the deconvolution of CV of signals. The former cathodic peak can be attributed to the single step reduction of Au^{3+} to Au°, whereas the latter might be due to the reduction of oxygen. This shifting of the oxygen reduction peak to a lower potential can be attributed to its facile reduction induced by the small deposit of Au° during CV scanning. AuNPs were deposited onto the Ti substrate by the potential step deposition method at − 0.85 V with varying deposition time, and a chronoamperometric current-time (*i-t*) plot for the deposition of AuNPs for 100 s is shown in Fig. S1.

Fig. 2b shows the CV of the AuNPs/Ti electrode (deposition time 100 s) in PB (pH 7.0) in the potential range between 0 and 1.0 V at a scan rate of 100 mV/s. The CVs of AuNPs/Ti electrodes with other deposition times are shown in Fig. S2. Bare Ti did not exhibit any redox activity in the potential scan range. AuNPs/Ti electrode clearly showed the formation of an AuO_x monolayer on the AuNPs, peaked at ca. 0.80 V (I) by positive polarization, which is reduced back at ca. 0.40 V (I′) during the reverse scan (Rahman et al., 2014). This was further verified by measuring the CV of the conventional Au electrode in PB (pH 7.0), as shown in the inset of Fig. 2b. This confirmed the successful deposition of AuNPs onto the Ti foil, which is evident in the photographic images of Ti and AuNPs/Ti electrodes (inset of Fig. 2b).

The electron transfer kinetics of the Ti and AuNPs/Ti electrodes were investigated by CV and EIS analysis, as shown in Figs. 2c and 2d, respectively. No redox activity for $[Fe(CN)_6]^{3-/4-}$ redox couple was observed at the Ti electrode. This can be attributed to the low conductivity (420 nΩ m at 20 °C) and low-catalytic activity of Ti. In contrast, the AuNPs/Ti electrode with the deposition time of 100 s exhibited a well-defined redox peak with the anodic (I_{pa}) and cathodic (I_{pc}) peak currents of ca. 158.1 and 151.97 μA, respectively, and the peak-to-peak potential separation (ΔE_{pp}) of ca. 0.15 V. This suggests high catalytic activity of AuNPs, which is consistent with previous reports (Rahman et al., 2014; Jo et al., 2017).

The EIS spectra of bare Ti electrode exhibited a very high (non-measurable) interfacial charge transfer resistance (R_{ct}) at the electrode|electrolyte interface for $[Fe(CN)_6]^{3-/4-}$ redox couple. This is well matched with the low-conductivity and catalytic activity of Ti. The AuNPs/Ti electrode displayed an ideal Nyquist plot with one semicircle at the high frequency region followed by an infinite Warburg diffusion resistance (W) at the low frequency region. The semicircle at the high frequency corresponded to the R_{ct} at the electrode|electrolyte interface, which was 5.25 kΩ for the AuNPs/Ti electrode. These EIS results are consistent with the CV results, and further indicate the high catalytic activity of AuNPs.

Further, we measured the CVs and EIS spectra of AuNPs/Ti electrodes with other deposition times (50, 75, and 150 s) (Fig. S3), and the corresponding numerical data are summarized in Figs. 2e and 2f, respectively. The AuNPs/Ti electrode with the AuNPs deposition time of 100 s exhibited the highest I_{pa}, lowest ΔE_{pp}, and R_{ct} for $[Fe(CN)_6]^{3-/4-}$ redox couple. Hereafter, the AuNPs/Ti electrode with the AuNPs deposition time of 100 s is considered the optimal electrode for further characterization and application, unless otherwise noted. The electrochemical stability of this optimized AuNPs/Ti electrode was analyzed by successive CV measurement for 10 cycles. The variation of I_{pa} of $[Fe(CN)_6]^{3-/4-}$ was very small with the relative standard deviation (RSD) of ca. 3.28%, indicating the excellent electrochemical stability of the electrode.

3.2. XRD and XPS characterization

X-ray diffraction (XRD) analyses were performed in order to investigate the crystallographic phases and structures of Ti and the AuNPs/Ti. Fig. 3a shows the XRD pattern of Ti and AuNPs/Ti in the 2θ range of 30–50°. Both of the electrodes exhibited the characteristic diffraction peaks of Ti at 2θ of ca. 35.15°, 38.45°, and 40.20°, which correspond to the (100), (002), and (101) planes, respectively, of the hexagonal close-packed (hcp) Ti (JCPSD#441294) (Premchand et al., 2006). However, the intensity ratios of all of the Ti peaks were varied significantly. This can be ascribed to the alteration of the preferred orientation/texture of Ti foil induced by the deposition of AuNPs (Barai et al., 2017). The AuNPs/Ti electrode exhibited additional peaks at ca. 37.64° and 43.87°, corresponding to the (111) and (200) planes of the face-centered cubic (fcc) Au (JCPDS#040784), respectively (Wang et al., 2011; Yenchalwar et al., 2014).

Additionally, the XPS spectra of Ti and AuNPs/Ti electrodes were measured so as to confirm the elemental composition and oxidation state of AuNPs. Fig. 3b displays the XPS narrow scan spectra of Au 4f in Ti and AuNPs/Ti electrodes. The corresponding survey spectrum is shown in Fig. S4. It is evident that the Ti electrode did not reveal any peak in the binding energy range of Au 4f, while the AuNPs/Ti electrode exhibited the Au 4f split peaks at ca. 84.17 and 87.88 eV. These correspond to the Au $4f_{7/2}$ and Au $4f_{5/2}$ doublet, respectively, which are close to the widely used reference values of Au° (84.0 and 87.7 eV, respectively) (Chenakin and Kruse, 2016; Azzouzi et al., 2015). This specifies the effective electrochemical reduction of Au^{3+} to Au° and the successful deposition of metallic AuNPs onto the Ti sheet.

3.3. Morphological analysis

Figs. 4a and 4b show the top-view FE-SEM images of bare Ti and AuNPs/Ti electrodes, respectively. The bare Ti electrode displayed a smooth surface with a low surface area, which is consistent with the previous report (Liu et al., 2014). In contrast, the AuNPs/Ti electrode with the AuNPs deposit for 100 s clearly showed the successful

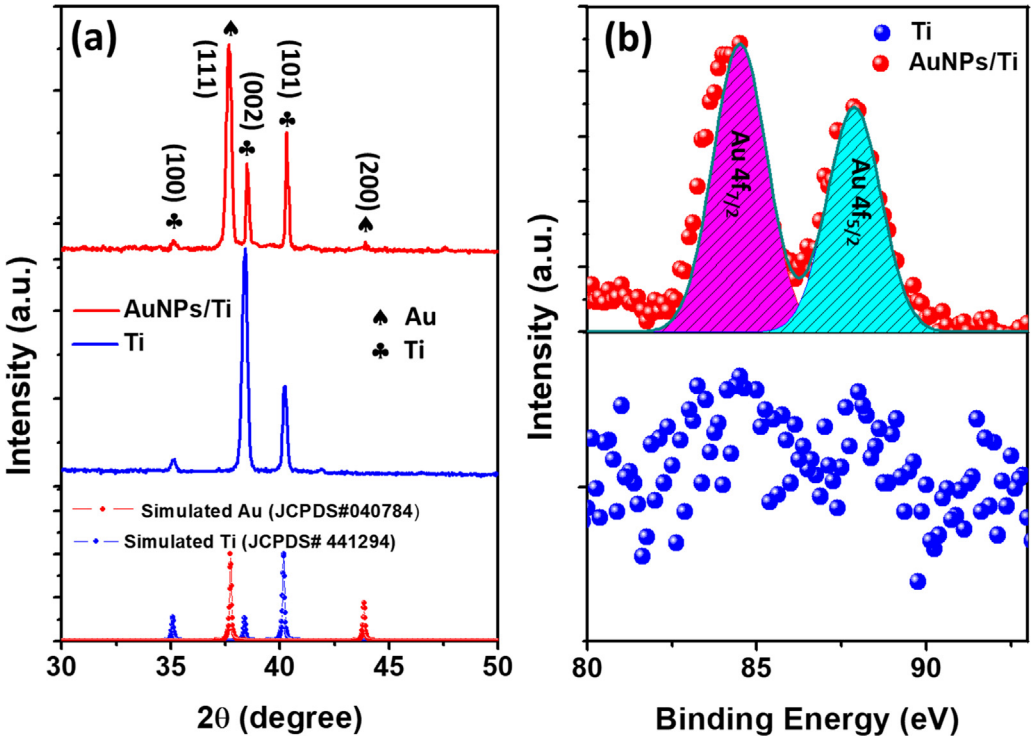

Fig. 3. (a) X-ray diffraction patterns of Ti and AuNPs/Ti. (b) XPS narrow scan spectra of Au 4f in Ti and AuNPs/Ti. The symbols and the shaded color regions indicate the experimental and fitting data, respectively.

deposition of nanoparticles with the average particle size of ca. 20 nm. The FE-SEM images of the AuNPs/Ti electrodes with other deposition times are shown in Fig. S5. This indicated that the particle densities and particle sizes were varied with increasing deposition time. FE-SEM images further specify that the electrochemical deposition of AuNPs onto Ti obeyed the progressive nucleation mechanism, followed by the growth and coalescence of the existing nuclei with the formation of additional nuclei (Rahman et al., 2014). The EDS spectra and elemental mapping of AuNPs/Ti electrode (Figs. S6 and S7) with the deposition time of 100 s further confirmed the deposition of pure AuNPs with the Au elemental wt% of 1.25. Figs. 4c and 4d show the topographical AFM images of bare Ti and AuNPs/Ti electrodes, respectively, which are consistent with the corresponding FE-SEM images. The deposition of AuNPs onto the Ti electrode enhanced its surface area from 7.0 to 18.30 μm^2, as calculated by AFM analyses.

In order to further characterize the morphologies and crystallographic patterns of AuNPs with HR-TEM, we detached the AuNPs from the Ti substrate in PB (pH 7.0) by vigorous sonication of the AuNPs/Ti electrodes. Fig. 4e shows the HR-TEM image of AuNPs, which indicates the formation of AuNPs with variable size, and it is consistent with the FE-SEM and AFM analyses. The SAED pattern exhibited the bright spots of the (111) and (200) planes, indicating the high crystallinity of AuNPs (inset of Fig. 4e). The inter-planar spacing between the adjacent fringes of AuNPs was ca. 0.24 nm (Fig. 4f), which is close to the calculated *d* spacing from the XRD measurement for the (111) diffraction plane, and is also consistent with previous reports (Bramhaiah et al., 2016; Premkumar et al., 2011). In additional, we measured the UV–Visible absorption spectrum of AuNPs (Fig. S8), which exhibited the characteristic absorption maxima of AuNPs at ca. 536.87 nm (Nealon et al., 2012).

3.4. Electrochemical characterization of the aptasensor

Figs. 5a and 5b show the CVs and EIS spectra, respectively, of the electrodes in a mixture solution of $[Fe(CN)_6]^{3-/4-}$. The I_{pa} was decreased from ca. 158.1 to ca. 110.97 μA after the immobilization of aptamer (1 μM) onto the AuNPs/Ti electrode with the increase of the ΔE_{pp} from ca. 0.15 to 0.35 V. The decrease of the electrocatalytic activity of $[Fe(CN)_6]^{3-/4-}$ at the Apt./AuNPs/Ti sensor is attributed to the improved electrostatic repulsion between the negatively-charged $[Fe(CN)_6]^{3-/4-}$ with the negatively-charged PO_4^{3-} backbone in the 3′ position of the aptamer (Rahman et al., 2015, 2016; Jo et al., 2015). This confirmed the successful immobilization of aptamers onto the electrode surface. This was further verified by measuring the HR-TEM image of the aptamer-immobilized AuNPs, as shown in Fig. S9, which indicates that AuNPs were covered by a monolayer of the aptamers. The I_{pa} of $[Fe(CN)_6]^{3-/4-}$ was decreased further to ca. 77.84 μA following the attachment of cTnI (500 pM) onto the Apt./AuNPs/Ti sensor surface with the ΔE_{pp} of ca. 0.44 V. This is due to the additional charge perturbation induced by the negatively charged $[Fe(CN)_6]^{3-/4-}$ and negatively charged cTnI (Jo et al., 2015; Peronnet et al., 2007). This specifies the effective binding of cTnI onto the sensor surface, indicating the high specificity of the sensor. These CVs results were consistent with the variation of the interfacial charge transfer resistance (R_{ct}) of the electrodes obtained from the EIS spectra, which were ca. 5.25, 8.15, and 15.95 kΩ at AuNPs/Ti, Apt./AuNPs/Ti, and cTnI/Apt./AuNPs/Ti, respectively.

3.5. Detection of cTnI and interference studies

Fig. 5c shows the DPV responses of $[Fe(CN)_6]^{3-/4-}$ oxidation after the attachment of cTnI at the Apt./AuNPs/Ti sensors with varying concentrations. The I_{pa} of $[Fe(CN)_6]^{3-/4-}$ oxidation was decreased with increasing cTnI concentrations. This is due to the aforementioned charge perturbation induced by the negatively-charged $[Fe(CN)_6]^{3-/4-}$ and negatively-charged cTnI (Jo et al., 2015; Peronnet et al., 2007). The I_{pa} was decreased with the increase of the concentration of cTnI from 1 to 1100 pM in PB (pH 7.0), which corresponds to a linear relationship between the I_{pa} and [cTnI] with a linear regression equation of I_{pa} (μA) = − (0.09 ± 0.00126) [cTnI](pM) + 152.22 ± 1.05 (R^2 = 0.997). This corresponds to a detection limit (S/N = 3) and sensitivity of 0.18 pM and 0.09 μA/pM, respectively. The analytical performance of

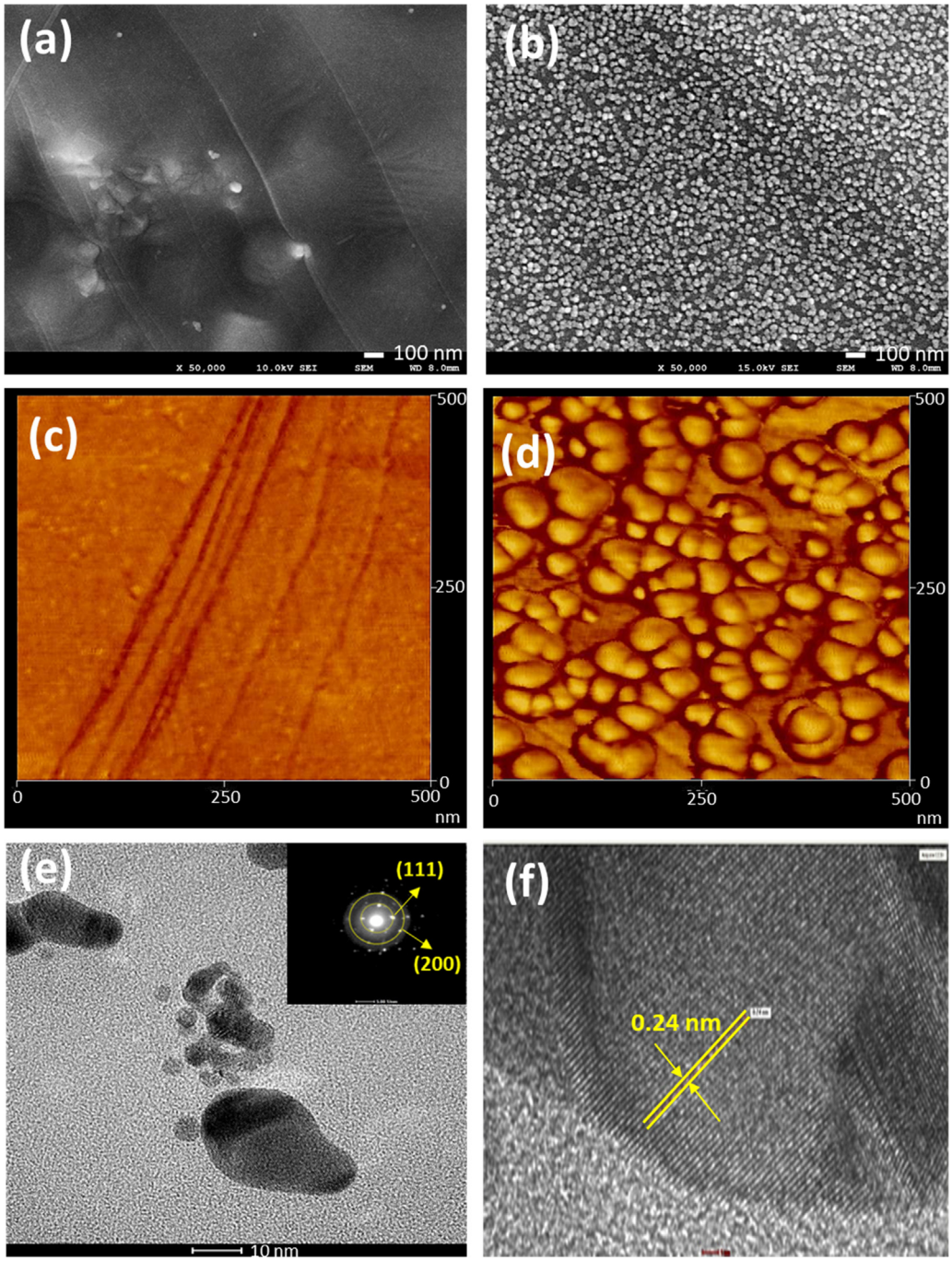

Fig. 4. FE-SEM images of (a) bare Ti and (b) AuNPs/Ti. Tapping mode AFM images of (c) bare Ti and (d) AuNPs/Ti. (e) HR-TEM image (inset shows the SAED pattern of AuNPs) and (f) lattice fringes of AuNPs.

this sensor is much better than the reported aptasensors (Jo et al., 2015, 2017; Negahdary et al., 2017) and immunosensors and is also better/comparable to other methods (e.g., optical, piezoelectric, colorimetric etc.) for the detection of cTnI, as summarized in Table S1. Thus, the aptasensor is highly sensitive for the detection of cTnI.

The selectivity of the current aptasensor was investigated using some possible interfering compounds, including Chol., BSA, Mb, GO_x, Ins., and IgG, each with the concentration of 1000 pM in PB (pH 7.0). Fig. 5d shows the variation of the I_{pa} of $[Fe(CN)_6]^{3-/4-}$ as the percentage of 500 pM cTnI binding current at the Apt./AuNPs/Ti sensor after incubating in different interfering compounds. The corresponding DPV responses are shown in Fig. S10. The interfering compounds do not significantly alter the I_{pa}, and the maximum I_{pa} was decreased by ca. 12.4% for Ins., indicating the high specificity and selectivity of the sensor for the detection of cTnI.

3.6. Stability, reproducibility, reusability, and real sample analyses

The stability of the sensor was tested by consecutive DPV measurements (seven times) for $[Fe(CN)_6]^{3-/4-}$ oxidation with a cTnI (500 pM)-attached Apt./AuNPs/Ti sensor. The variation of the I_{pa} was significantly low with the relative standard deviation (RSD) of ca. 2.88%, representing the high stability of the sensor. Additionally, the Apt./AuNPs/Ti sensor retained ca. 94.70% of its initial response after being stored in PB (pH 7.0) at 4 °C for seven days. The reproducibility of the sensor was verified by the DPV measurements for $[Fe(CN)_6]^{3-/4-}$

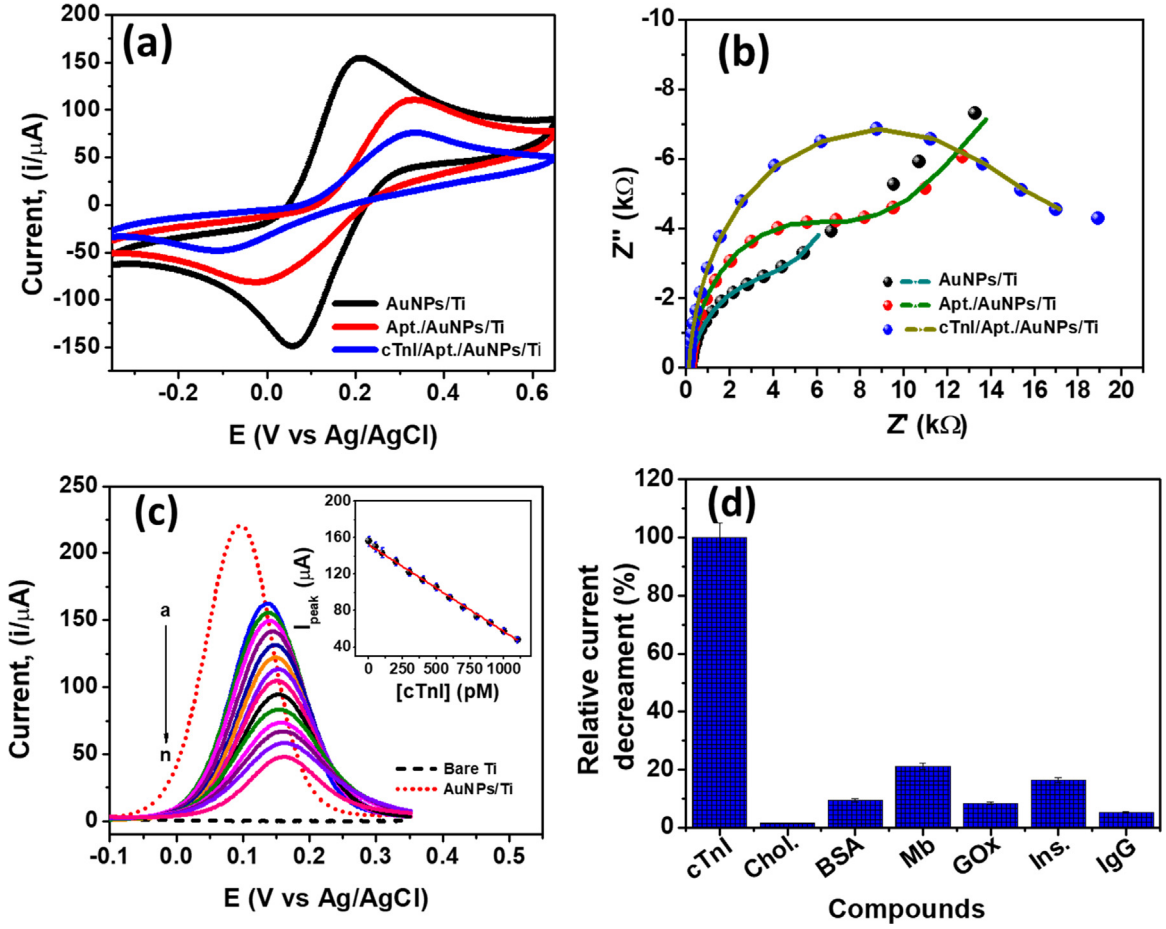

Fig. 5. (a) CVs (b) and EIS spectra of AuNP/Ti, Apt./AuNPs/Ti, and cTnI/Apt./AuNPs/Ti electrodes in $[Fe(CN)_6]^{3-/4-}$ solution. The scan rate for CV measurement was 100 mV/s. All of the EIS spectra were fitted with the equivalent circuit model, as shown in the inset of Fig. 2(d). The symbols and solid lines in the EIS spectra indicate the experimental and fitted data, respectively. (c) DPV responses of $[Fe(CN)_6]^{3-/4-}$ oxidation at different concentrations (a→h: 0, 1, 50, 100, 200, 300, 400, 500, 600, 700, 800, 900, 1000, and 1100 pM) of target cTnI attached Apt./AuNPs/Ti sensors together with the DPVs of bare Ti and AuNPs/Ti electrodes (inset shows the plot of I_{pa} vs. [cTnI]). (d) Relative variation of the I_{pa} after the binding of possible interfering compounds and cTnI.

oxidation at five independent cTnI (500 pM) attached sensors, which showed the RSD of ca. 1% for I_{pa} (Fig. S11).

The reusability of the aptasensor was investigated by breaking the complex formed between the aptamer and cTnI. This was achieved by dipping the cTnI-attached (500 pM) aptasensor into a 0.1 M $HCl_{(aq.)}$ solution for 10 min at 25 °C, in accordance with a previous report (Radi et al., 2006). The results revealed that the I_{pa} of $[Fe(CN)_6]^{3-/4-}$ oxidation was decreased significantly after acid treatment (ca. 74.37%, 65.10%, and 45.74%, respectively) compared to the I_{pa} values of AuNPs/Ti, Apt./AuNPs/Ti, and cTnI/Apt./AuNPs/Ti electrodes. The significant reduction of the I_{pa} value of cTnI/Apt./AuNPs/Ti is possibly due to the corrosion of Ti metal induced by HCl (Zhong et al., 2017). This can remove the AuNP and aptamers from the sensor surface, which ultimately destroyed the sensor assembly. Thus, the present aptasensor cannot be reused with the current methodology. However, the aptasensor is still promising for the development of a disposable type POCT system for cTnI.

PB (pH 7.0) diluted (100 times) human serum (Sigma-Aldrich) samples were used as real samples in order to investigate the practical applicability of the sensor. This was tested by incubating the sensors in real samples containing 100 and 500 pM of cTnI. The I_{pa} of DPVs (Fig. S12) were compared with an external calibration plot (Fig. S13) after the attachment of cTnI, and the results are summarized in Table S2. The average relative recoveries for 100 and 500 pM of cTnI were 100.20% and 101.80%, respectively. This indicates that the present aptasensor is capable of detecting cTnI in real biological samples with high accuracy, and it is promising for pathological studies.

4. Conclusions

In summary, we developed a simple, sensitive, and selective aptamer-based electrochemical cTnI detection assay based on AuNPs modified Ti foil. AuNPs were deposited onto a Ti foil with nanosize, homogenous distribution, high-density, and purity through the potential step deposition method. A cTnI binding thiolated aptamer was immobilized onto the optimized AuNPs/Ti electrode via the covalent bonding of S-Au, which decreased the I_{pa} of $[Fe(CN)_6]^{3-/4-}$ and increased R_{ct}. The I_{pa} of the redox probe was decreased further when cTnI was attached onto the sensor surface. After the binding of cTnI, the I_{pa} was decreased further with increasing concentrations of cTnI, which showed a linear behavior in a wide concentration range (1–1100 pM). As a result, the aptasensor showed high sensitivity and a low detection limit (ca. 0.18 pM) for the detection of cTnI. The aptasensor displayed high stability, reproducibility, interference-free signals, and good recoveries of cTnI in human serum samples. Although the sensor cannot be reused in our investigated methodology, it is promising for the development of a disposable type POCT system for the early accurate screening and diagnosis of AMI. It is expected that the current fabrication method will serve as a promising diagnostic tool for numerous diseases.

Acknowledgments

This work was supported by the National Research Foundation of Korea (NRF), grant funded by the Korea government (MSIP) (2016R1A2B4010600) and by the Small and Medium Business Administration (SMBA) and Korea Institute for Advancement of Technology (KIAT) through the World Class 300 project R&D.

Appendix A. Supplementary material

Supplementary data associated with this article can be found in the online version at doi:10.1016/j.bios.2018.11.012.

References

Azzouzi, S., Rotariu, L., Benito, A.M., Maser, W.K., Ali, M.B., Bala, C., 2015. Biosens. Bioelectron. 69, 280–286.
Ahammad, A.J.S., Choi, Y.-H., Koh, K., Kim, J.-H., Lee, J.-J., Lee, M., 2011. Int. J. Electrochem. Sci. 6, 1906–1916.
Barai, H.R., Rahman, M.M., Joo, S.W., 2017. Electrochim. Acta 253, 563–571.
Bramhaiah, K., Singh, V.N., John, N.S., 2016. Phys. Chem. Chem. Phys. 18, 1478–1486.
Bakir, Ç., Şahin, N., Polat, R., Dursun, Z., 2011. J. Electroanal. Chem. 662, 275–280.
Brady, W.J., Roberts, D., Morris, F., 1999. Am. J. Emerg. Med. 17, 394–397.
Chekin, F., Vasilescu, A., Jijie, R., Singh, S.K., Kurungot, S., Iancu, M., Badea, G., Boukherroub, R., Szunerits, S., 2018. Sens. Actuators B-Chem. 262, 180–187.
Chenakin, S.P., Kruse, N., 2016. Phys. Chem. Chem. Phys. 18, 22778–22782.
Christenson, E., Christenson, R.H., 2013. Ann. Lab. Med. 33, 309–318.
Davies, K.R., Gelb, A.W., Manninen, P.H., Boughner, D.R., Bisnaire, D., 1991. Br. J. Anaesth. 67, 58–63.
Fonseca, R.A., Ramos-Jesus, J., Kubota, L.T., Dutra, R.F., 2011. Sensors 11, 10785–10797.
GBD 2015 Disease and Injury Incidence and Prevalence Collaborators, 2016. Lancet 388, 1545–1602.
Han, X., Li, S., Peng, Z., Othman, A.M., Leblanc, R., 2016. ACS Sens. 1, 106–114.
Jo, H., Her, J., Lee, H., Shim, Y.-B., Ban, C., 2017. Talanta 165, 442–448.
Jo, H., Gu, H., Jeon, W., Youn, H., Her, J., Kim, S.-K., Lee, J., Shin, J.H., Ban, C., 2015. Anal. Chem. 87, 9869–9875.
Ko, S., Kim, B., Jo, S.-S., Oh, S.Y., Park, J.-K., 2007. Biosens. Bioelectron. 86, 51–59.
Korff, S., Katus, H.A., Giannitsis, E., 2006. Heart 92, 987–993.
Lopa, N.S., Rahman, M.M., Ahmed, F., Sutradhar, S.C., Ryu, T., Kim, W., 2018a. Electrochim. Acta 274, 49–56.
Lopa, N.S., Rahman, M.M., Ahmed, F., Sutradhar, S.C., Ryu, T., Kim, W., 2018b. Microchim. Acta 185, 23.
Liu, R., Gu, S., Du, H., Li, C.M., 2014. J. Mater. Chem. A 2, 17263–17267.
Mendis, S., Puska, P., Norrvingm, B., 2011. Global Atlas on Cardiovascular Disease Prevention and Control.
Min, K., Cho, M., Han, S.Y., Shim, Y.B., Ku, J., Ban, C., 2008. Biosens. Bioelectron. 23, 1819–1824.
Maehashi, K., Katsura, T., Kerman, K., Takamura, Y., Matsumoto, K., Tamiya, E., 2007. Anal. Chem. 79, 782–787.
Negahdary, M., Behjati-Ardakani, M., Sattarahmady, N., Yadegari, H., Heli, H., 2017. Sens. Actuators B-Chem. 252, 62–71.
Nealon, G.L., Donnio, B., Greget, R., Kappler, J.-P., Terazzi, E., Gallani, J.-L., 2012. Nanoscale 4, 5244–5258.
Premkumar, T., Lee, K., Geckeler, K.E., 2011. Nanoscale 3, 1482–1484.
Peronnet, E., Becquart, L., Martinez, J., Charrier, J.-P., Jolivet-Reynaud, C., 2007. Clin. Chim. Acta 377, 243–247.
Premchand, Y.D., Djenizian, T., Vacandio, F., Knauth, P., 2006. Electrochem. Commun. 8, 1840–1844.
Ritchie, H., Roser, M., 2018. Causes of Death.
Rezaee, M.A., Rasaee, M.J., Mohammadnejad, J., 2017. J. Immunoass. Immunochem. 38, 72–81.
Rahman, M.M., Lopa, N.S., Kim, Y.J., Choi, D.-K., Lee, J.-J., 2016. J. Electrochem. Soc. 163, B153–B157.
Rahman, M.M., Kim, Y.J., Lee, J.-J., 2015. J. Electrochem. Soc. 162, B159–B162.
Rahman, M.M., Li, X.-B., Lopa, N.S., Lee, J.-J., 2014. Bull. Korean Chem. Soc. 35, 2072–2076.
Radi, A.-E., Sánchez, J.L.A., Baldrich, E., O'Sullivan, C.K., 2006. J. Am. Chem. Soc. 128, 117–124.
Tang, M., Zhou, Z., Shangguan, L., Zhao, F., Liu, S., 2018. Talanta 180, 47–53.
Tuteja, S.K., Chen, R., Kukkar, M., Song, C.K., Mutreja, R., Singh, S., Paul, A.K., Lee, H., Kim, K.-H., Deep, A., Suri, C.R., 2016. Biosens. Bioelectron. 86, 548–556.
Tombelli, S., Minunni, M., Mascini, M., 2005. Biosens. Bioelectron. 20, 2424–2434.
Wang, Z., Zhao, S., Zhu, S., Sun, Y., Fang, M., 2011. CrystEngComm 13, 2262–2267.
Yenchalwar, S.G., Azhagan, V.K., Shelke, M.V., 2014. Phys. Chem. Chem. Phys. 16, 17786–17791.
Yang, Z., Zhou, D.M., 2006. Clin. Biochem. 39, 771–780.
Zhong, X., Yu, S., Hu, J., Chen, L., Shi, Y., Zhang, Z., Gao, S., Zeng, D., Shi, T., 2017. Int. J. Electrochem. Sci. 12, 2875–2892.